Supplemental Information

S1 Information on Local Meteorological Stations and Inter-comparison with Modular Station Wind Data

Table S1 Location and hourly measurement capabilities of air quality and meteorology monitoring stations in the Sarnia Region. Stations with * are operated by the Sarnia-Lambton Environmental Association (SLEA).

Name	Latitude (Degrees)	Longitude (Degrees)	NO_x	O_3	SO_2	10m-Wind	Solar Irradiance
Aamjiwnaang	42.91255	-82.4168	✓	✓	✓	✓	
*Front Street	42.9706	-82.4098	✓	✓	✓	✓	
*LaSalle Road	42.91133	-82.3799			✓	✓	
*Moore Line	42.83954	-82.4208				✓	✓
*RiverBend	42.87735	-82.4545	✓	✓	✓	✓	
Sarnia (MOECC)	42.990263	-82.395341	✓	✓	✓		
*Sombra Line	42.741413	-82.43549			✓		
*Scott Road	42.94978	-82.3972			✓	✓	

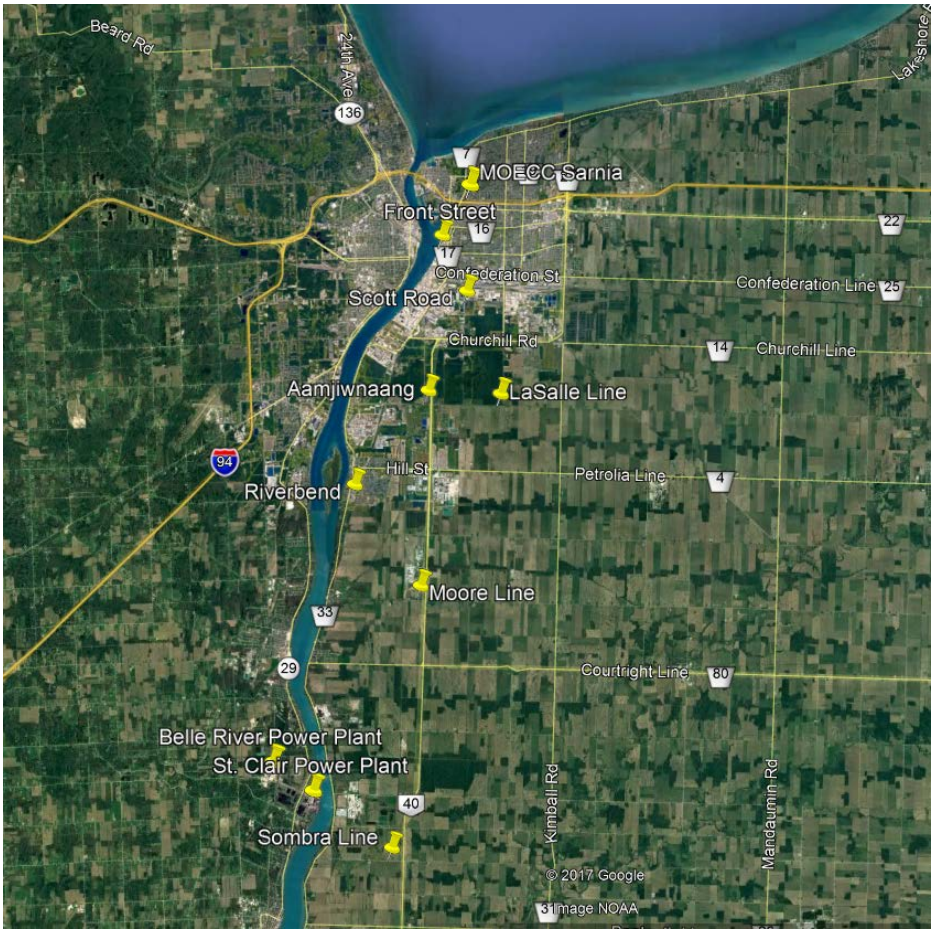

Figure S1 Locations of Air Quality and Monitoring Stations in Sarnia-Lambton Region.

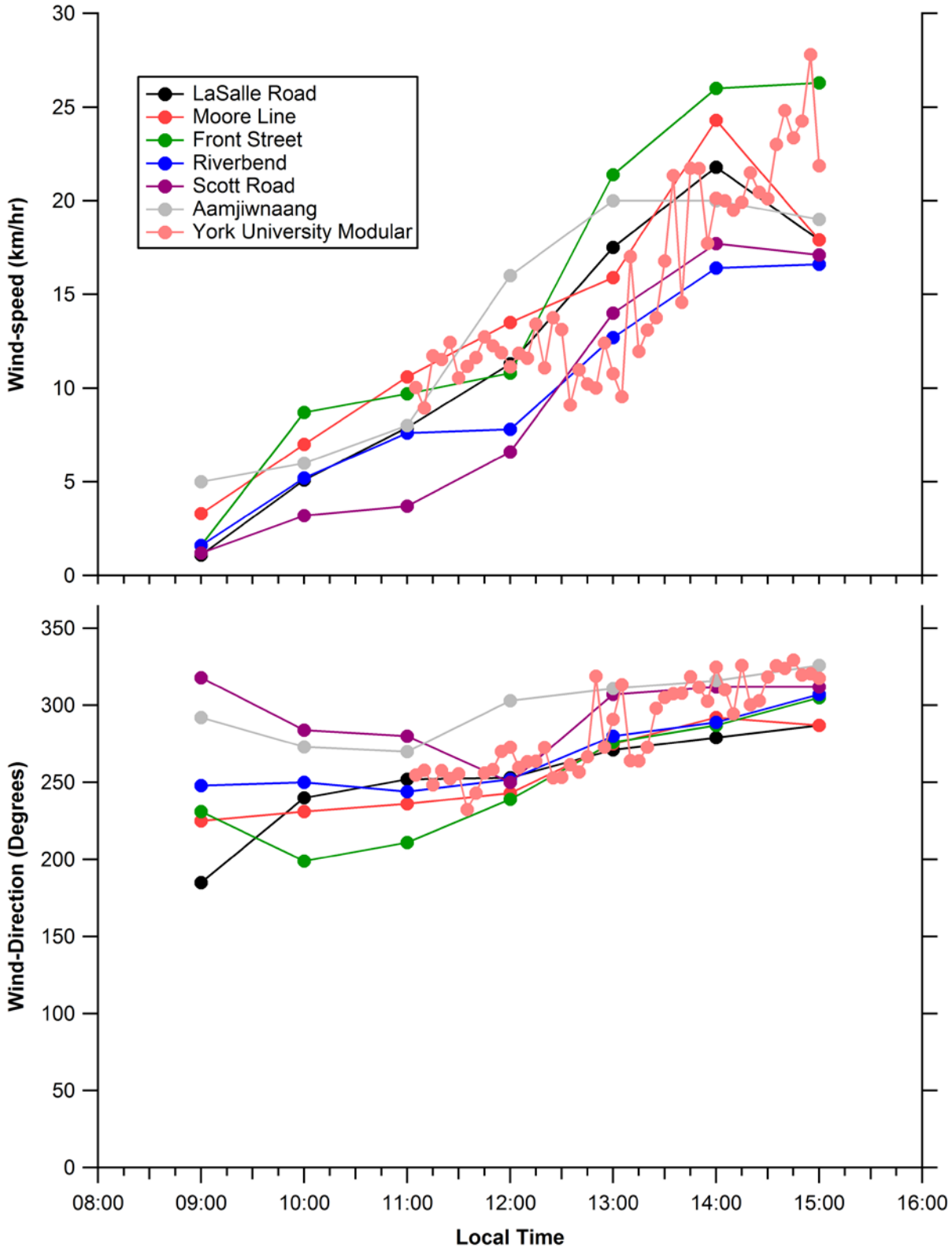

Figure S2 Day1 wind-speeds (top) and wind-directions (bottom) from permanent stations (hourly average) and 5-minute average from the modular meteorological station.

S2 WRF model setup and Inter-comparison of Results with Observed Winds

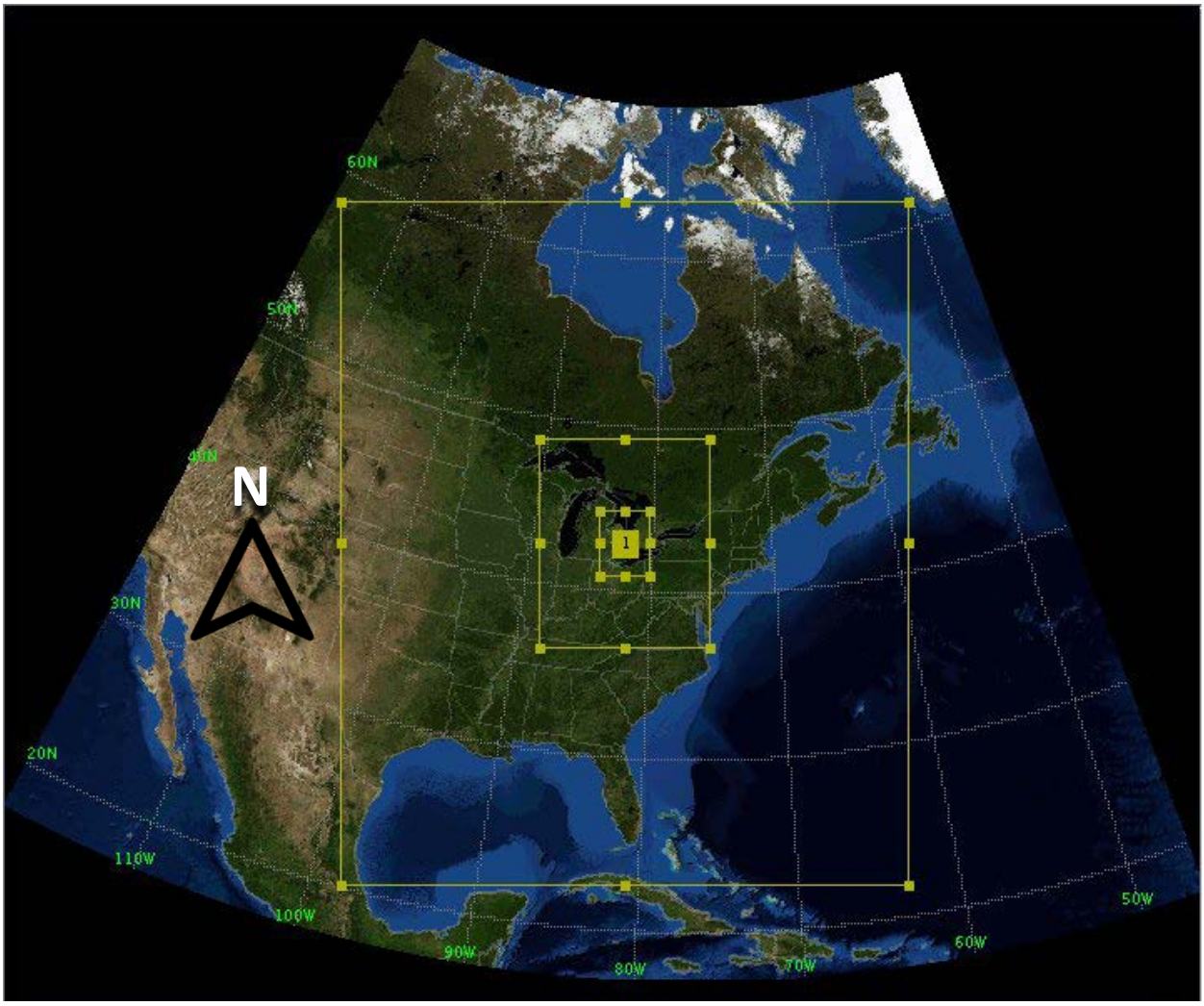

Figure S3 WRF modelled domains centred on Sarnia, Ontario.

S2.1 WRF Model Setup

WRF was set up using a series of nested domains (Fig. S3) centred on Sarnia, Ontario (42.9745N, 82.4066W) at 27 km, 9 km, 3 km and 1 km horizontal resolutions from the outer to innermost domains. The model had 30 vertical levels up to 100 hPa. Surface-layer physics was represented by the Monin-Obukhov scheme. Initial and lateral boundary conditions were provided using the North American Regional Reanalysis (NARR) data product, which includes assimilated meteorological observations from the North American network. Simulations were conducted using both the Yonsei University (YSU) and Mellor–Yamada–Janjic (MYJ) boundary-layer physics schemes. The YSU scheme was chosen for inter-comparison with observed winds because in literature comparisons of multiple schemes, YSU had the smallest mean bias for winds-speed and RMSE and was found to have greater consistency with observed boundary layer variables compared to local schemes such as MYJ (Banks et al., 2016; Fekih and Mohamed, 2017). Simulations of vertical profiles of winds in similar terrain to our study (relatively flat terrain close

to a water body) found that YSU performed better under unstable conditions compared to MYJ, which performed better under stable conditions (Draxl et al., 2014). YSU was used in our study because estimates of atmospheric stability conditions during our measurements suggest slightly unstable or neutral conditions (see Supplement S3, Table S2). The MYJ scheme was also tested to determine whether the boundary layer scheme choice made a significant impact on the modelled wind results. The YSU and MYJ schemes produced very similar modelled wind-speed and –direction results.

S2.2 Inter-comparison of Wind-Speeds and –Directions from WRF and Station Observations.

Figures S4-S6 show inter-comparisons of hourly wind-speeds and wind-directions at La Salle Road and Moore Line station locations from MOECC observations and modelled at 1km resolution using WRF. WRF modelled wind-directions for Day 1 frequently deviated from the observed hourly values by ~75^{o} (Fig. S4). WRF wind-speeds in the 0-20 m layer for Day 1 were ~2-4 times the observed 10 m winds during daylight hours (Fig. S4). Overestimation of observed 10 m winds by WRF is fairly typical, but the magnitudes of the Root Mean Square Error (RMSE) for Days 1 and 2 of 4.8 m s^{-1} and 3.9 m s^{-1}, respectively, are larger than found in literature; 2-3 m s^{-1} (Banks et al., 2016; Draxl et al., 2010; Shin et al., 2012). The magnitude of the RMSE for Day 1 is greater than the wind-speeds observed while driving. Even assuming that the YSU scheme performs better during unstable conditions, which are more likely to occur during the daytime, the RMSE for daylight hours is still 4.6 m s^{-1} for Day 1. Even accounting for the typical decrease in wind-speed bias and RMSE with increasing altitude (Banks et al., 2016; Draxl et al., 2010, 2014), the WRF wind-speeds within the first 200 m are unrealistically large on Day 1 given power-law (P-L) modelled vertical profiles of wind-speeds scaled using the observed 10 m wind-speeds (Supplement S3). The P-L profiles indicate that under the possible atmospheric stability conditions, wind-speeds aloft would not be as high as the modelled winds based on the measured near-surface speeds. The P-L vertical wind-speed profiles were not used to calculate emissions for reasons discussed in Supplement S3.

Modelled winds for Day 2 at LaSalle Road station overestimated measured winds, which is somewhat expected based on literature, but Moore Line station modelled winds were frequently 30-40% smaller than 10 m measured winds in the 0-40 m layers, which simply suggests poor model performance (Fig. S5). Day 3 wind-speeds modelled by WRF were more consistent with observed wind-speeds compared to Day 1 or 2 results, but modelled wind-directions still deviated by ~30-40^{o} during the morning (driving period) at both stations (Fig. S6).

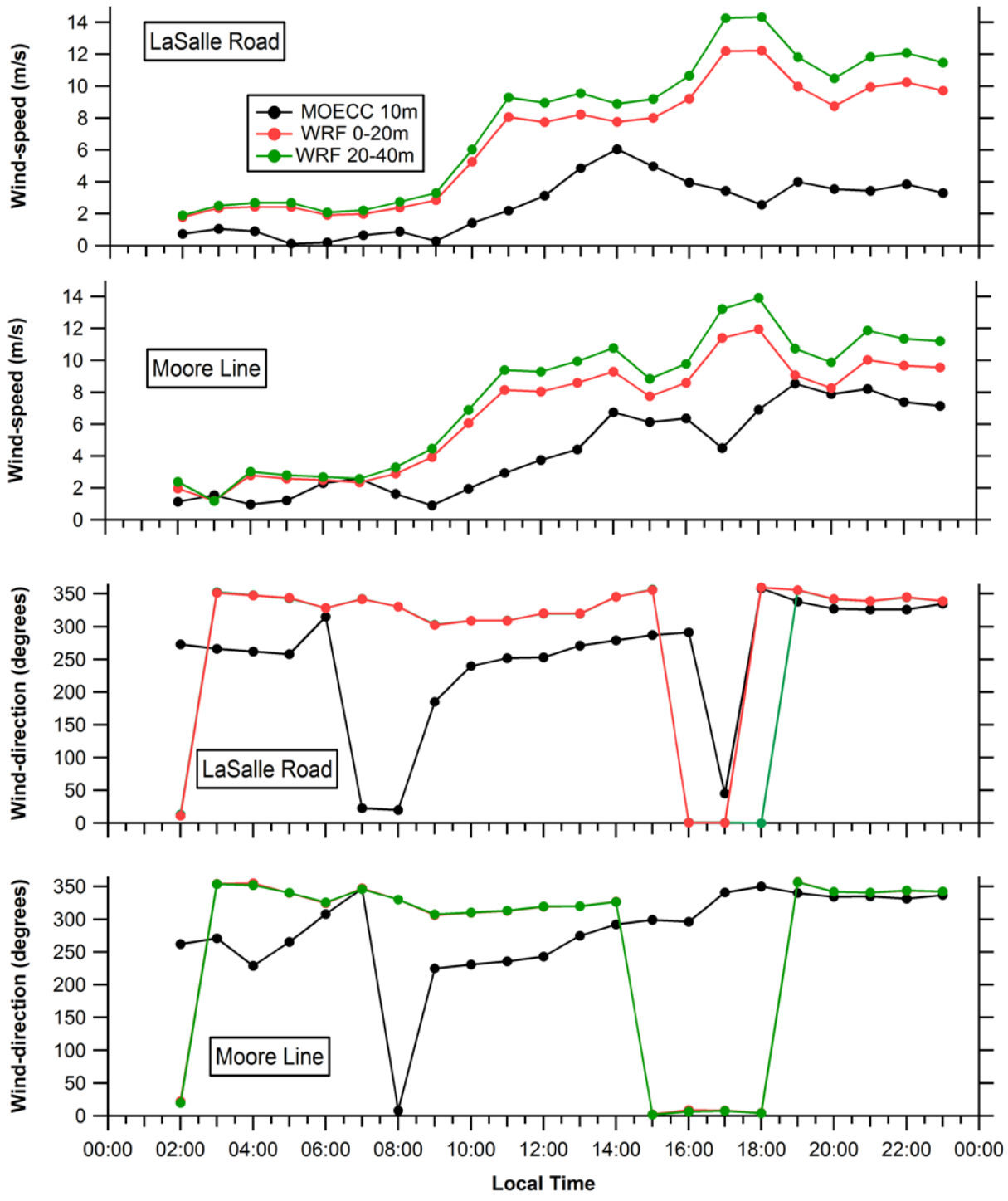

Figure S4 Day 1 comparison of hourly average wind-speeds and -directions from WRF modelling and MOECC measurements at La Salle Road and Moore Line locations.

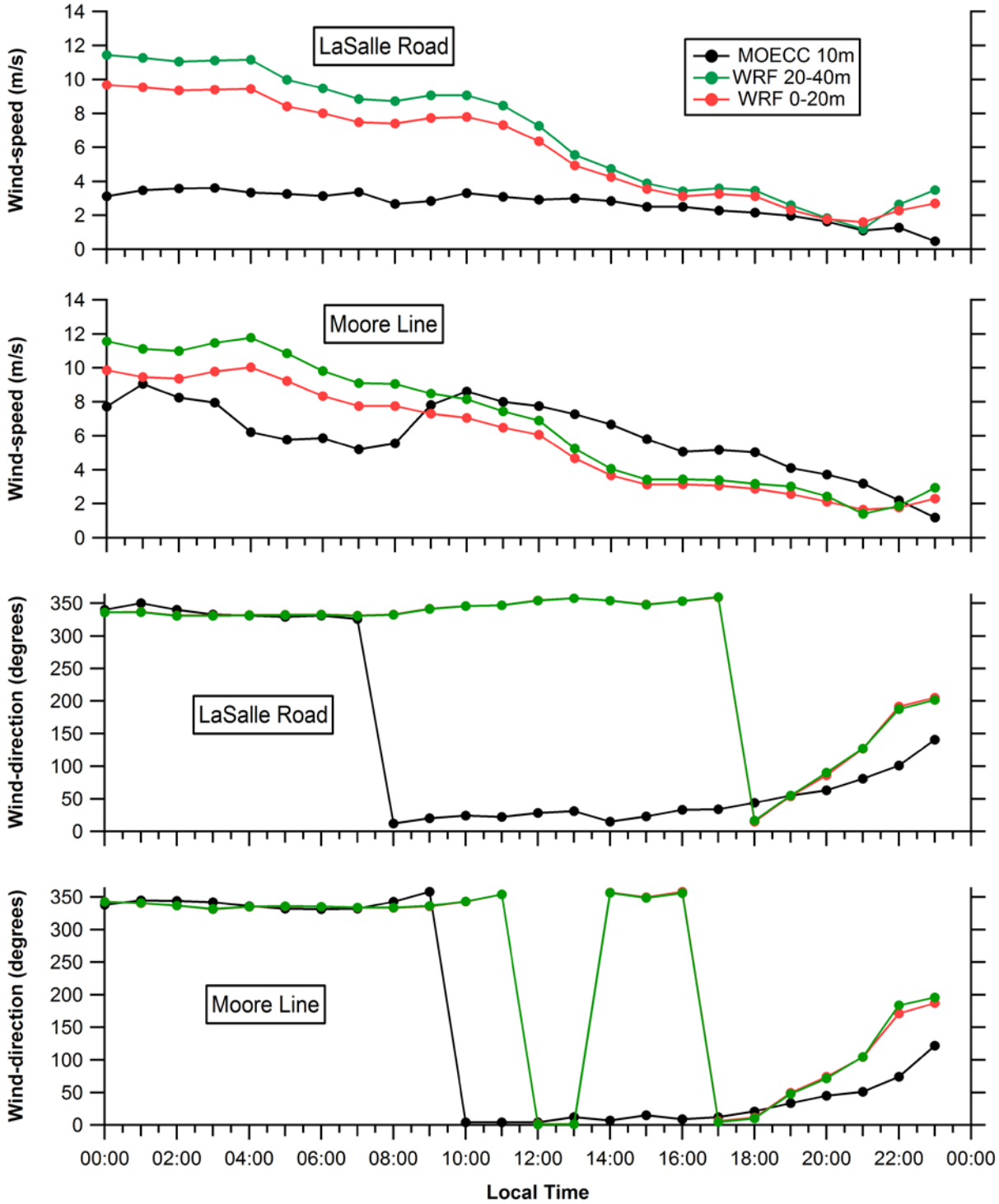

Figure S5 Day 2 comparison of hourly average wind-speeds and -directions from WRF modelling and MOECC measurements at La Salle Road and Moore Line locations.

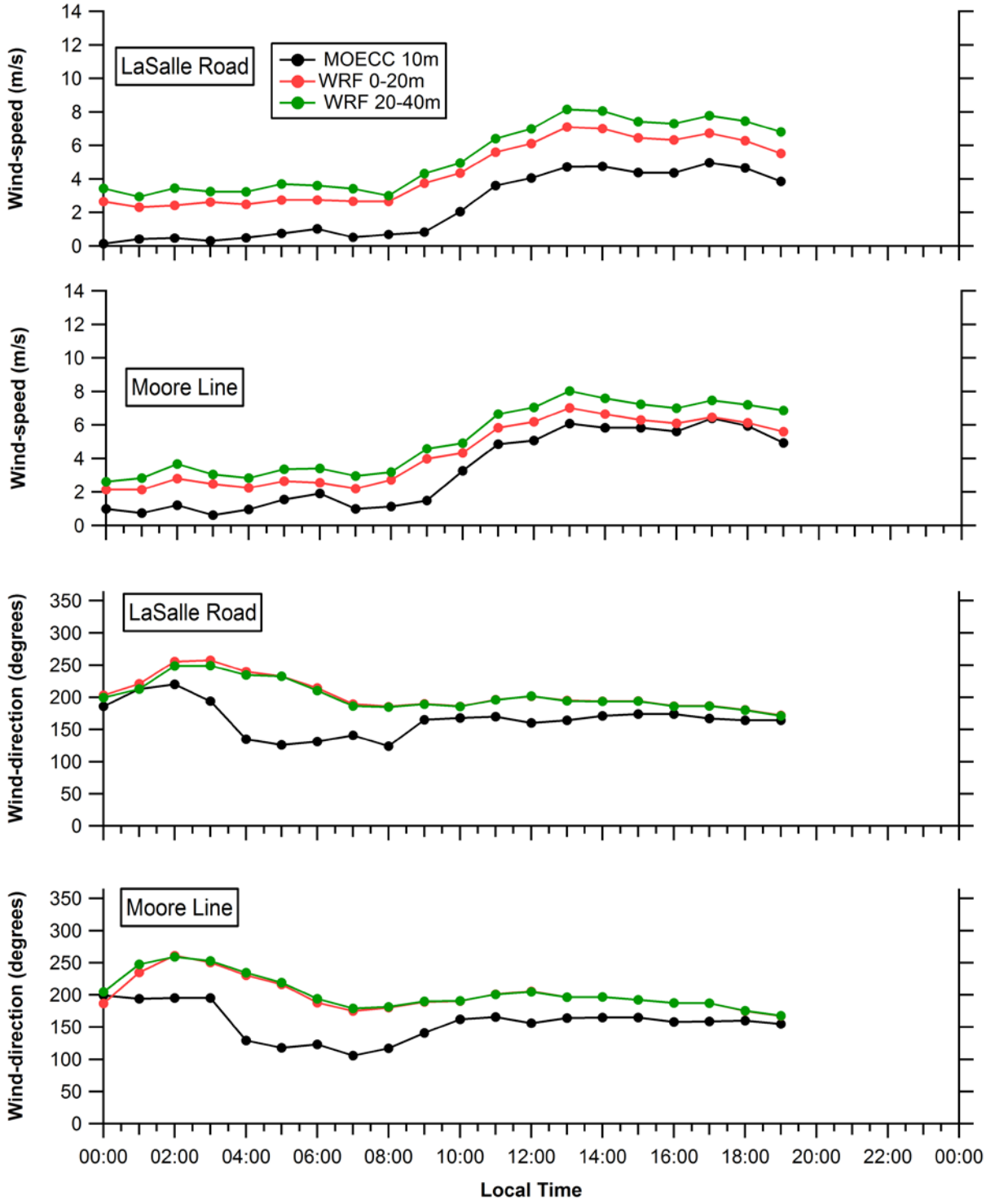

Figure S6 Day 3 comparison of hourly average wind-speeds and -directions from WRF modelling and MOECC measurements at La Salle Road and Moore Line locations.

S3 Vertical Wind Profile Estimation using the Power Law Function

Vertical wind profiles can be estimated using a power law function.

$$\boldsymbol{U_{PL}(z) = U_n \left(\frac{z}{z_o}\right)^p} \quad \text{(S1)}$$

Where $U_{PL}(z)$ is the wind-speed at height z, z_o is the reference height, U_n is the wind-speed at height z_o and p is the power-law index (PLI). U_n is the measured 10 m wind-speed from the local monitoring stations in this study. The PLI depends on atmospheric stability and roughness of the terrain (e.g., flat fields versus cities with many obstructions) (Kikumoto et al., 2017) as seen in Table S2.

Table S2 Power-Law Exponents (PLI) for Urban and Rural Wind Profiles (EPA, 2000)

Stability Class	Definition	Urban PLI	Rural PLI
A	Very Unstable	0.15	0.07
B	Unstable	0.15	0.07
C	Slightly Unstable	0.2	0.10
D	Neutral	0.25	0.15
E	Slightly Stable	0.3	0.35
F	Stable	0.3	0.55

More stable atmospheric conditions or urban landscapes tend to produce wind-speed profiles that increase more rapidly with altitude while unstable conditions or rural landscapes tend to produce more vertically uniform profiles. The P-L model is not used to estimate emissions because this profile was designed to model high-speed winds under neutral atmospheric stability conditions for structural engineering applications (Kikumoto et al., 2017) and is generally only applicable to <200 m while plumes may be expected at 500m+ in this study. Also, the accuracy of the P-L profile has been shown to decrease with short time intervals (e.g., < 1 hour) under low wind-speed (Kikumoto et al., 2017) such as those observed during most of the measurement periods in this study. The PLI can also depend on the height interval within <200 m (Hanafusa et al., 1986) so that different height levels may need to be modelled separately.

Table S3 P-G Stability Class from the Horizontal Standard Deviation of Wind-Direction and SRDT Method for Routes on Day 1 to Day 3.

Day	Transect	P-G Stability Class: σ_A Method	SRDT Method
1	1	N/A	C
1	2	C/D	C
1	3	C/D	B/C
2	1	D	C
3	1	D	C
3	2	D	C

In order to estimate the PLI, atmospheric stability (Pasquill-Gifford (PG) stability class) was estimated using the hourly horizontal wind-direction standard deviations σ_a measured by the modular meteorological station and adjusted for the wind-speed using hourly average LaSalle Road station data. The hourly standard deviation is computed using a pooled standard deviation from four 15-minute σ_a using the eq (S2) (EPA, 2000).

$$\boldsymbol{\sigma_{a,1-hr}} = \left[\frac{(\boldsymbol{\sigma_{a1}})^2 + (\boldsymbol{\sigma_{a2}})^2 + (\boldsymbol{\sigma_{a3}})^2 + (\boldsymbol{\sigma_{a4}})^2}{\mathbf{4}}\right]^{\mathbf{1/2}} \quad \text{(S2)}$$

The stability category was also estimated using the SRDT method, which is based on down-welling solar radiation and wind-speed (EPA, 2000). Hourly average solar radiation data was from the Moore Line station. The stability classes estimated using the two methods are shown in Table S3. However, based on these methods the P-G may have been either C (slightly unstable) or D (neutral) for all three days. The wind-speeds and/or horizontal wind-direction standard deviations were close to the border of the range of values for the two categories. The PLI was estimated using both C and D stability classes assuming a rural location in all cases since there were few obstructions between the measurement locations and the sources, especially for Day 3 (EPA, 2000).

S4 Estimation of Non-Industrial NO_x Emissions from Port Huron and Sarnia

S4.1 Day 1 Port Huron Vehicular Emission Estimate

Vehicular NO_x emissions from Port Huron were estimated using traffic counts and vehicular NO_x emission factors in order to estimate NO_x influx from Port Huron and to validate the influx VCD choice. Average daily traffic counts for 2016 were obtained from the MDOT Interactive map of Port Huron (Michigan Department of Transportation, n.d.). The map provides total traffic counts and commercial traffic, allowing an estimation of the proportion of cars to trucks. This estimation is important because trucks are much more likely to have diesel engines with significantly higher NO_x emission factors. Emissions from major roads in the Port Huron area that likely impacted the measurements were included, including sections of highways 94 and 69. This estimate does not take into account the vehicular emissions that occur on small roads in Port Huron but these emissions are expected to be relatively small compared to the commercial truck emissions in this area.

The NO_x vehicular emission fluxes strongly depend on the NO_x emission factor assumed for cars and trucks. NO_x emission factors vary significantly depending on vehicle type and age with older vehicles generally emitting more NO_x per mile. Gasoline car NO_x emission factors ranged from 0.06 to 2.38 gNO_x $mile^{-1}$ based on measurements by Carslaw et al. (2011) and heavy-duty vehicle NO_x emission factors range from 12.4 to 26 gNO_x $mile^{-1}$ based on measurements in Vancouver's Cassiar Connector highway traffic tunnel (Rogak et al., 1998). The estimate assumes all non-commercial vehicles were gasoline cars and heavy-duty vehicles included semis, cube vans and dump trucks. In order to convert daily NO_x emissions to hourly NO_x emissions to compare to the Mobile-MAX-DOAS emission estimates, the vehicle emissions were assumed to occur within 12 hours of a day since less vehicular activity occurs at night. Depending on the NO_x emission factor used, the total vehicular emission estimate range was 0.03-0.25 tonnes h^{-1} The yearly contribution range is 230-1100 tonnes yr^{-1}. This range is reasonable given

the 2011 emissions of NO_x from Hamilton, Ontario were estimated to be ~4000 tonnes (McMaster Institute for Transportation and Logistics, 2014) and that the population of Port Huron is ~1/20 of Hamilton's population.

S4.2 Estimate of Sarnia Area Non-Industrial Emissions

2015 total Ontario NO_x emissions were 311 kilotonnes with ~82% of those emissions due to non-industrial sources (i.e., transportation, residential and utilities). Non-industrial Ontario emission may be estimated to be 255 kilotonnes in 2015. Sarnia non-industrial emission can be estimated by scaling the Ontario non-industrial emissions of 255 kilotonnes yr^{-1} by the area of Sarnia relative to the area of all Ontario cities, giving an estimate of ~1270 tonnes yr^{-1}.

S5 Sensitivity of Emission Estimates to VCD_{influx} Value

Tables S4, S5, S6 and S7 show the sensitivity of the NO_x and SO_2 emissions to different values of background VCD influx. Emission estimates from Day 3 were calculating using the local average transect background VCD values and assuming constant VCD_{influx} values of 1 $x10^{15}$ and 0.5 $x10^{15}$ molec cm^{-2}. However, the emission estimates using the local average VCDs from each transect are likely the most accurate because the VCD in the background upwind of NOVA Chemicals is expected to be low and relatively constant. Also, since a local FRS was used to retrieve the DSCDs in each case, assuming a constant background VCD for all transects likely introduces error since the NO_2 present in each FRS would vary but is negated if the average background VCD is used.

Table S4 Day 1 NO_x emissions calculated with a range of influx NO_2 VCD values.

NO_2 VCD_{influx} ($x10^{15}$ molec cm^{-2})	Route 1 NO_x emission (tonnes h^{-1})	Route 2 NO_x emission (tonnes h^{-1})	Route 3 NO_x emission (tonnes h^{-1})
0.5	1.99	1.65	1.74
1	1.86	1.42	1.63
1.5	1.74	1.29	1.52
2	1.61	1.17	1.41
3	1.37	0.91	1.19
Average	1.71	1.29	1.50
Standard Deviation	0.24	0.28	0.21
Relative Standard Deviation	14%	22%	14%

Table S5 Day 2 lower limit NO_2 emissions calculated with zero and $1x10^{15}$ molec cm^{-2} VCD_{influx} values and constant and variable NO_x/NO_2 ratios.

Conditions	NO_x (tonnes h^{-1})
VCD_{influx} = 1 $x10^{15}$ molec cm^{-2} & NO_x/NO_2 = 1.47	1.50
VCD_{influx} = 0 & NO_x/NO_2 = 1.47	1.80
VCD_{influx} = 1 $x10^{15}$ molec cm^{-2} & Variable NO_x/NO_2	2.23
Average	1.83
Standard Deviation	0.37
Relative Standard Deviation	20%

Table S6 Day 3 lower limit NO_x emissions calculated using transect averaged background VCD influx values and influx values of $0.5x10^{15}$ and $1x10^{15}$ molec cm^{-2}.

NO_2 VCD_{influx}	Route 1 NO_x (tonnes h^{-1})	Route 2 NO_x (tonnes h^{-1})
Individual Transect Averages	0.67	0.69
$0.5x10^{15}$ molec cm^{-2}	0.91	1.23
$1x10^{15}$ molec cm^{-2}	0.52	0.95
Average	0.70	0.96
Standard Deviation	0.19	0.27
Relative Standard Deviation	27%	28%

Table S7 SO_2 lower limit emissions from Day 1 route 3 with varying background VCD values.

SO_2 VCD_{influx} ($x10^{15}$ molec cm^{-2})	SO_2 (tonnes h^{-1})
0.6	3.3
1.00	2.3
1.20	1.8
Average	2.47
Standard Deviation	0.76
Relative Standard Deviation	31%

S6 Conversion Factor Values for Estimating NO_x Emissions from NO_2 Emissions

Table S8 Conversion Factor Values for Estimating NO_x Emissions from NO_2 Emissions. Day 2 route 1* used individual NO_x/NO_2 values rather than a route-averaged value.

Day	Route	NO_2 to NO_x Emission Conversion Factor
1	1	2.52
1	2	1.80
1	3	1.69
2	1	1.52
2	1*	2.26
3	1	1.49
3	2	1.52

S7 Error Estimates and Sensitivity Analysis

Sensitivity analysis was conducted for routes by varying the NO_x/NO_2 ratio, lifetime, wind-direction, and (Day 1 only) VCD_{influx} values (Table S9). The error listed in Table S9 for each of these factors is the maximum percentage variation of the emission estimate using the standard value to the most different emission value produced using the range of values. The route respective average NO_x/NO_2 values were varied by ±1 standard deviation, the lifetime was varied between 4 and 8 hours, the route respective wind directions were varied by ±10° and the influx VCDs for

Day 1 were varied from 0.5 to $3x10^{15}$ molec cm^{-2} for NO_2 and 0.6 to $1.23x10^{15}$ molec cm^{-2} for SO_2. VCD_{influx} error on Day 2 was presumed to be similar to Day 1 on since no usable background VCD measurements were available. VCD_{influx} error for Day 3 was presumed to be the same as the VCD_{geo} error for each transect since there was little variation in the local background values. Since the emission values were calculated as lower limit estimates given 10 m wind-speed, wind-speed error was not included. SO_2 DSCD error was higher due to greater detection limit and lower sensitivity compared to NO_2.

Table S9 Error contributions to emission estimates. * Indicates assumed value rather than from tested variability.

Gas	NO_x	NO_x	NO_x	NO_x	NO_x	NO_x	SO_2
Day	1	1	1	2	3	3	1
Route	1	2	3	1	1	2	3
DSCD	15%	15%	15%	15%	15%	15%	30%
VCD_{geo}	20%	20%	20%	20%	20%	20%	20%
NO_x/NO_2 ratio	5%	5%	5%	5%	10%	10%	N/A
Lifetime	30%	12%	12%	7%	2%	2%	N/A
Wind-Speed	N/A	N/A	N/A	N/A	N/A	N/A	N/A
Wind-Direction	22%	15%	15%	6%	12%	12%	15%
VCD_{influx}	18%	29%	19%	*25%	*20%	*20%	30%
NO_x/NO_2 CL errors	5%	5%	5%	5%	5%	5%	0
Total Error	49%	43%	37%	37%	36%	36%	46%

S8 Relative Seasonal OH Production and Derivation of the Leighton Ratio Equation

S8.1 Derivation of the Production of OH

OH is produced though reaction of $O(^1D)$, produced from photolysis of O_3, with H_2O.

$$\boldsymbol{O_3 + h\nu \rightarrow O_2 + O(^1D)} \quad \text{(S3)}$$

$$\boldsymbol{O(^1D) + M \rightarrow O + M} \quad \text{(S4)}$$

$$\boldsymbol{O(^1D) + H_2O \rightarrow 2OH + O_2} \quad \text{(S5)}$$

Given Eqs. F1-F3 the production rate of OH is:

$$\boldsymbol{P_{OH} = 2k_5[O(^1D)][H_2O]} \quad \text{(S6)}$$

Where concentration is denoted by square brackets, k_5 is the rate constant for reaction (S5). Assuming $\boldsymbol{O(^1D)}$ is in steady-state, the production of OH depends on the concentrations of O_3 and H_2O.

$$\mathbf{P_{OH} = \frac{2J_{O3}k_5}{k_4[M] + k_5[H_2O]}[O_3][H_2O]} \quad \text{(S7)}$$

Where J_{O3} is the photolysis rate constant for O_3 and k_2 is the rate constant for Reaction (S3). At typical atmospheric H_2O mixing ratios the term $\mathbf{k_5[H_2O]}$ is small compared to the term $\mathbf{k_4[M]}$, allowing the approximation (Seinfeld and Pandis, 2016):

$$\boldsymbol{P_{OH} \approx \frac{2J_{O3}k_5}{k_4[M]}[O_3][H_2O]} \quad \text{(S8)}$$

Therefore, $\boldsymbol{P_{OH}\ \alpha [O_3][H_2O]}$.

Table S10 Comparison of $[H_2O]*[O_3]$ product during summer conditions and study (spring) conditions. Temperature, Relative Humidity and $[O_3]$ from SLEA Front Street Station.

Date (2017)	Local Time	Temperature (^oC)	Relative Humidity	O_3 (ppb)	O_3 (x10^{11} molec cm^{-3})	$[H_2O]*[O_3]$ (10^{29} $molec^2$ cm^{-6})	$[H_2O]*[O_3]_{spring}$ / $[H_2O]*[O_3]_{summer}$
1-Jul	10:00	23	0.74	29	7.2	3.6	
1-Jul	11:00	24.1	0.68	33	8.1	4.0	
1-Jul	12:00	25	0.61	37	9.1	4.3	
21-Mar	10:00	7.8	0.53	10	2.6	0.38	0.10
21-Mar	11:00	11	0.3	22	5.7	0.57	0.14
21-Mar	12:00	12.3	0.29	32	8.2	0.86	0.20

The product of H_2O and O_3 was calculated assuming $O(^1D)$ was in steady-state. The daytime spring-conditions products for Days 1 and 2 are approximately 10-20% of the summertime product determined from Front Street SLEA monitoring data on 01/06/2017.

S8.2 Leighton Ratio Derivation

During the daytime troposphere, NO_2 is photolyzed to form NO and an $O(^3P)$ atom.

$$\boldsymbol{NO_2 + h\nu \rightarrow NO + O(^3P)} \quad \text{(S9)}$$

The $O(^3P)$ atom reacts with molecular oxygen to form O_3 in a three-body reaction.

$$\boldsymbol{O(^3P) + O_2(+M) \rightarrow O_3(+M)} \quad \text{(S10)}$$

The O_3 can then reform NO_2 from NO.

$$\boldsymbol{NO + O_3 \rightarrow NO_2 + O_2} \quad \text{(S11)}$$

When O_3 is in photostationary state, the mixing ratio of O_3 depends on the NO and NO_2 concentrations via the following equation:

$$\boldsymbol{[O_3] = (J[NO_2])/(k_{11}[NO])} \quad \text{(S12)}$$

Where J_{NO2} and k_{11} are the photolysis rate of NO_2 and the rate constant for reaction (S11), respectively.

The Leighton ratio ($\boldsymbol{\phi}$) is produced by dividing both sides of the equation by $[O_3]$

$$\boldsymbol{\phi = \frac{J_{NO2}[NO_2]}{k_8[NO][O_3]}} \quad \text{(S13)}$$

The value of $\boldsymbol{\phi}$ tends to be unity in regions with high NO_x levels but be greater than unity when other chemical processes convert NO to NO_2 other than the reaction of NO with O_3 (Griffin et al., 2007).

S9 Discarded Route: Day 1 Route 4

A fourth route on Day 1 (Fig. S7) was driven during conditions that violated the constant wind-field assumptions.The prevailing wind direction was Westerly (284^{o}) during the route, but there were periods of rapid wind-direction fluctuation between 270^{o} (Westerly) to 313^{o} (North-North-Westerly) (Fig. S8), which was deemed to be too variable. An emission estimate calculated from this route would thus depend on what portion of the route was driven at what time, rather than on the emission rate. For this reason, an emission estimate was not calculated for this route. These results highlight the importance of obtaining high temporal resolution wind measurements to achieve accurate Mobile-MAX-DOAS emission estimates.

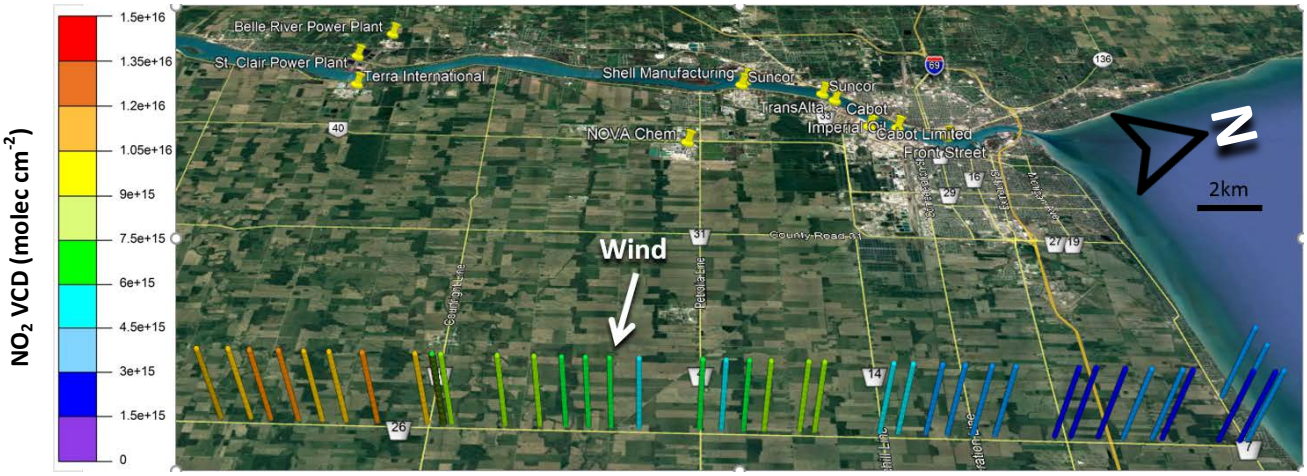

Figure S7 Day 1 Route 4 NO_2 VCDs.

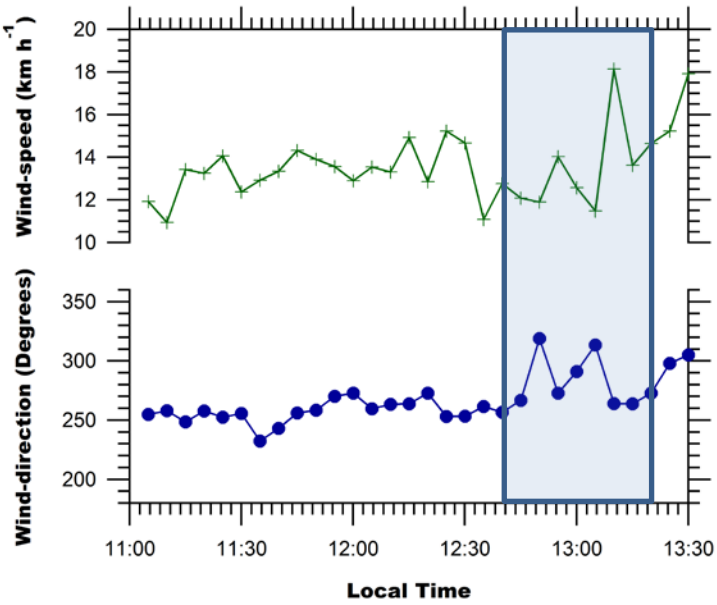

Figure S8 Wind-speed and -direction (5-minute average) from the modular meteorological station on Day 1.